

Modeling analysis of tidal bore formation in convergent estuaries

Andrea Gilberto Filippini (*Corresponding author*)

*Team CARDAMOM, Inria Bordeaux sud-Ouest and IMB, - 200 av. de la vieille tour,
33405 Talence cedex, France*

Luca Arpaia

*Team CARDAMOM, Inria Bordeaux sud-Ouest and IMB, - 200 av. de la vieille tour,
33405 Talence cedex, France*

Philippe Bonneton

*CNRS, UMR EPOC, University of Bordeaux, Allée Geoffroy Saint-Hilaire, 33615 Pessac
cedex, France*

Mario Ricchiuto

*Team CARDAMOM, Inria Bordeaux sud-Ouest and IMB, - 200 av. de la vieille tour,
33405 Talence cedex, France*

Abstract

Despite the recognized impact of tidal bores on estuarine ecosystems, the large scale mechanism of bore formation in convergent alluvial estuaries is still under investigation. So far, field data exist only for a small number of estuaries, while numerical simulations employ the shallow water equations mainly focusing on the small-scale and local processes. In this work, firstly we apply the fully nonlinear weakly dispersive Serre-Green-Naghdi equations to simulate the tide propagation in a convergent estuary of idealized form, verifying that the local dispersion effects, responsible for the appearance of the secondary waves, do not influence the tidal bore onset, which only results from the large scale processes of amplification/damping and distortion of the incoming wave. In

Email addresses: andrea.filippini@inria.fr (Andrea Gilberto Filippini (*Corresponding author*)), luca.arpaia@inria.fr (Luca Arpaia), p.bonneton@epoc.u-bordeaux1.fr (Philippe Bonneton), mario.ricchiuto@inria.fr (Mario Ricchiuto)

a second part, we numerically investigate (225 runs) the estuarine parameter space in order to identify the physical conditions that lead to tidal bore generation. In this parameter space, we determine a critical curve which divides estuaries according to tidal bore occurrence. As a result of this investigation we have shown that bore formation is controlled by the competition between two physical processes: a) the *knee-shaped* distortion of the tidal wave, with flood dominance and eventually bore inception; b) the dissipation of the tidal wave, which is unfavorable to bore formation. We also provide evidence that amplification due to topographic convergence is not a necessary condition for tidal bore generation and that there exist estuaries which display both wave damping and bore development. Finally, the validity of the results has been also assessed in the presence of freshwater river discharge, showing that for low river discharge, its effect on estuarine dynamics can be neglected.

Keywords: Estuarine hydrodynamics; long wave; tidal bore formation; dispersion; undular tidal bore; Serre-Green-Naghdi equations.

1. Introduction

Tidal wave transformation in convergent alluvial estuaries plays a crucial role in the development of a sustainable management of water resources. For this reason, and to better understand the human impact on the estuarine ecosystem, it has been the subject of intensive scientific research. Parametric studies conducted in [1, 2, 3, 4, 5] have shown that, when neglecting river discharge effects, the estuarine hydrodynamics is controlled by only three dimensionless parameters. These parameters represent a combination of the properties of the tidal forcing at the estuary mouth (wave amplitude and period), the large-scale geometrical characteristics of the channel and the friction coefficient. For particular conditions of the above dimensional variables, of freshwater flow and of river channel bathymetry, the tidal wave may result strongly distorted when the flow turn to rise, and a bore can be observed at the beginning of the flood tide. In the lower part of the estuary, tidal wave propagation can be well described by

15 the so called Saint Venant or Nonlinear Shallow Water (NLSW) equations with
16 friction (*cf.* [6]). However the onset of a tidal bore and its evolution upstream
17 is controlled by non-hydrostatic dispersive mechanisms (*cf.* [7]). Even if Mad-
18 sen *et al.* [8] and Pan and Liu [9] have shown that the non-dispersive NLSW
19 equations with shock capturing methods can still be used to simulate breaking
20 bore propagation with relatively good results, undular bores requires the use
21 of other long wave modeling approaches. If weakly dispersive weakly nonlinear
22 Boussinesq-type equations can be adopted to describe the onset of the tidal bore
23 (*cf.* [7]), the nonlinear evolution of high-intensity bores requests fully nonlinear
24 equations to be employed, as for example the Serre-Green-Naghdi (SGN) ones
25 (*cf.* [10, 11, 12]). The first part of this work is thus devoted to reproduce the
26 progressive formation of an undular tidal bore inside an idealized estuary using
27 the SGN equations.

28 The results obtained in this first part will then justify the use of the NLSW
29 model to investigate at large scales how the three dimensionless parameters,
30 which control the estuarine long scale dynamics, influence the physical pro-
31 cesses of amplification/damping and distortion which may lead to the bore on-
32 set. These processes take place at large spatial and temporal scales, where
33 the non-hydrostatic effects associated with tidal bores can be neglected. Some
34 numerical studies already used the NLSW system to simulate the propagation
35 of tidal waves in rivers up to bore formation, but they are limited to a single
36 [8, 9] or to a small number [4] of estuaries. A similar limitation concerns also
37 field data: since every estuary in nature represents a unique combination of the
38 three dimensionless variables, we dispose only of a limited number of points in
39 the parameter space coming from *in situ* measurements. Based on the set of
40 data available, it is very difficult to understand how such parameters influence
41 the bore development process. In this paper, we bypass this major constraint
42 through a numerical investigation of the whole space of dimensionless variables.
43 This allows us both to characterize the global conditions for tidal bore occur-
44 rence and to analyze for each estuarine regime the nonlinear processes associated
45 with tidal wave transformation. Our approach is based on a scaling analysis in-

46 introduced in [13], where the reader can also find a collection of estuary data,
47 which are used here to validate our numerical investigation.

48 The paper is structured as follows: section 2 introduces the idealized ge-
49 ometry used to accomplish our study and defines the dimensionless parameters
50 emerging from the scaling analysis of the governing equations; section 3 gives
51 some details about the solution strategy adopted to solve the SGN system, the
52 implemented numerical scheme and motivates the choice of the type of bound-
53 ary conditions used; section 4 introduces a criterion for bore detection based
54 on experimental observation *in situ*; the numerical simulation of the onset of an
55 undular tidal bore inside an idealized estuary is presented in section 5; section 6
56 discusses the numerical investigation on the favorable conditions for tidal bore
57 occurrence, introducing a criterion for bore detection based on experimental
58 observation *in situ* and showing the main findings of the study; finally, section
59 7 treats the effects of water river discharge on tidal bore formation.

60 2. Problem setting

61 The study of tidal wave propagation in funnel shaped estuaries is often per-
62 formed under several simplifying assumptions. The geometry of real alluvial
63 estuaries in coastal plains can be well-approximated by an exponentially de-
64 creasing width variation and flat bathymetry [14, 15, 6]. This morphology is
65 the natural result of a morphodynamic equilibrium of the erosion/sedimentation
66 process. For this reason, we will perform our study on the simplified case (figure
67 1) of a tide propagating in an idealized convergent channel of constant depth
68 D_0 and an exponentially decreasing width $B(x)$, varying in the longitudinal
69 direction x with the law:

$$B(x) = B_0 e^{-x/L_b} \quad (1)$$

70 where L_b represents the convergence length of the channel. We assume a rect-
71 angular cross-section suitable, as a first approximation, to describe the behavior
72 of a real section with the same area.

73

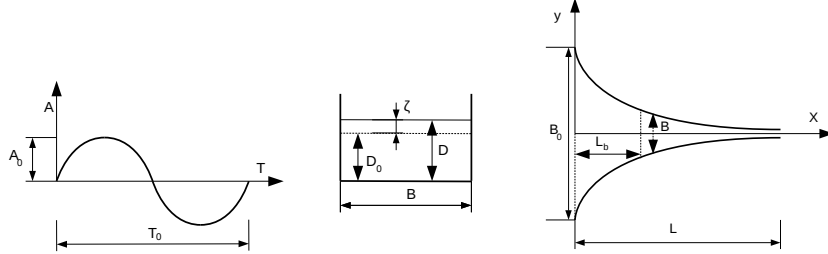


Figure 1: Sketch of the idealized geometry of the channel and basic notations.

74 It is a common practice in the literature to use quasi-one-dimensional sys-
 75 tems of equations to investigate the large scale dynamics of long waves propa-
 76 gating in convergent channels [1, 2, 16, 5, 4]. In the case of open channels with
 77 exponentially decreasing cross section areas, the equations assume the following
 78 form:

$$\begin{aligned} \frac{\partial \zeta}{\partial t} + u \frac{\partial \zeta}{\partial x} + D \frac{\partial u}{\partial x} - \frac{uD}{L_b} &= 0 \\ \frac{\partial u}{\partial t} + u \frac{\partial u}{\partial x} + g \frac{\partial \zeta}{\partial x} + C_{f0} \frac{u|u|}{D} &= 0 \end{aligned} \quad (2)$$

79 where $D = \zeta + D_0$ denotes the total water depth, with ζ the free surface elevation
 80 and D_0 the still water depth and u stands for the cross-sectionally averaged flow
 81 velocity. The friction term is modeled by a quadratic law, with C_{f0} the friction
 82 coefficient.

83 As already remarked by others in the literature [1, 2, 4, 13] three external
 84 dimensionless parameters appears to fully control the system (2). Following the
 85 scaling of the equations proposed by Bonneton *et al.* [13], these parameters are:

$$\epsilon_0 = \frac{A_0}{D_0}, \quad \delta_0 = \frac{L_{w0}}{L_b}, \quad \phi_0 = \frac{C_{f0}(gD_0)^{1/2}}{\omega_0 D_0}; \quad (3)$$

87 where D_0 , A_0 and ω_0 form a set of reference external parameters, respectively
 88 the water depth, the amplitude and the angular frequency of the tidal wave.
 89 Here ϵ_0 represents the standard nonlinearity parameter, δ_0 is the convergence
 90 ratio, ϕ_0 is a friction parameter and $L_{w0} = (gD_0)^{1/2} \omega_0^{-1}$ is the frictionless tidal-

91 wave length scale.

92 Field observations reported in [3] show that in tidal bore estuaries the tidal
93 wave nonlinearity is mainly characterized by the dimensionless parameter

$$D_i^* = \epsilon_0 \phi_0 / \delta_0 , \quad (4)$$

94 being always one order of magnitude greater than ϵ_0 .

95 Both theoretical studies [1] and experimental observations [3] agree that large
96 values of the dissipation parameter D_i^* produce great distortion and peaking of
97 the free surface and velocity profiles of the tidal wave, leading to flood domi-
98 nance; characteristics which correspond to necessary conditions for tidal bore
99 formation ($D_i^* \geq 1.7$ in [3]). However, large values of D_i^* correspond also to
100 high energy dissipation, leading to tidal damping; unfavorable to tidal bore for-
101 mation. For this reason some natural estuaries, despite having high values of
102 D_i^* , don't display a bore. In order to evaluate the relative importance of friction
103 in the momentum balance, several definitions of the friction parameter ϕ_0 have
104 been introduced in the literature [1, 2, 17, 4]. Although all of these definitions
105 are analogous from a physical point of view, only the one introduced by the
106 present authors in [13] allows to investigate separately the opposite effects of
107 peaking and dissipation taking place for high values of D_i^* . In this paper we
108 describe the details of the numerical investigation behind the scaling proposed
109 in [13]. We will thus explore numerically the space of the external parameters
110 ϵ_0 , δ_0 and ϕ_0 , quantifying which range of values is in favour of tidal bore for-
111 mation.

112 Considering that, for most alluvial estuaries, the convergence ratio δ_0 is close to
113 2 (as showed in figure 2 of [13]), we have chosen to perform our analysis using
114 a constant value $\delta_0 = 2$. Due to such a simplification, the expression of the
115 dissipation parameter (4) reduces to: $D_i^* = \alpha \epsilon_0 \phi_0$ (with α constant). Thus, it
116 is possible to investigate the separate effects of peaking and dissipation, both
117 contained in D_i^* , by numerically exploring only the plane of the dimensionless
118 parameters (ϕ_0 , ϵ_0). The effects of nonlinear dispersion and of the discharge are
119 also investigated, while we leave out for the moment the influence of bathymetric

120 variations.

121 **3. Numerical model**

122 *3.1. Governing equations*

123 For nonlinear long waves, a reasonably general description is provided by
 124 the fully nonlinear weakly dispersive Serre-Green-Naghdi equations. As already
 125 mentioned, this model allows to simulate the phenomenon in its entirety, includ-
 126 ing the nonlinear dispersive effects active on the smaller scales. To the authors'
 127 knowledge, it does not exist so far any mathematical model allowing to account
 128 for such effects in quasi-1D setting. The closest work is the very recent paper
 129 of Winckler and Liu [18], who developed a set of weakly nonlinear Boussinesq
 130 equations. This justifies the use of a full two-dimensional model. In particular,
 131 the SGN equations can be recast as [19, 20]:

$$\frac{\partial \zeta}{\partial t} + \nabla \cdot (D \mathbf{u}) = 0, \quad (5a)$$

$$\frac{\partial u}{\partial t} + (\mathbf{u} \cdot \nabla) \mathbf{u} + g \nabla \zeta + C_{f0} \frac{\mathbf{u} |\mathbf{u}|}{D} = \boldsymbol{\psi}, \quad (5b)$$

$$(\mathbf{I} + \mathbf{T}) \boldsymbol{\psi} = \mathbf{T} \left(g \nabla \zeta - C_{f0} \frac{\mathbf{u} |\mathbf{u}|}{D} \right) - \mathbf{Q}(\mathbf{u}); \quad (5c)$$

132 where \mathbf{u} is the depth averaged velocity vector of horizontal component u and
 133 transversal one v , $\boldsymbol{\psi}$ characterizes the non-hydrostatic and dispersive effects,
 134 and the linear operators $\mathbf{T}(\cdot)$ and $\mathbf{Q}(\cdot)$ are the same defined in [20] and their
 135 expressions are given in appendix A.

136 It is worth noting that, when applying the scaling proposed in [13] and recalled
 137 in section 2 to system (5) (details are reported in appendix A), an additional
 138 dimensionless parameter $\mu^2 = (D_0/L_0)^2$ appears into the equations, multiply-
 139 ing all the dispersive terms (*cf.* equation (17b)). This parameter is responsible
 140 for the fact that the non-hydrostatic effects become negligible when the charac-
 141 teristic scale of the phenomenon is large, transforming the original SGN system
 142 of equations into the non-conservative form of the Non-Linear Shallow Water
 143 (NLSW) system. For this reason, dispersion does not influence significantly

144 the large scales of tidal wave propagation, which can be well described by the
145 NLSW equations. A direct verification of this is given and discussed in section 5.

146

147 *3.2. Numerical strategy*

148 To solve system (5) we adopt the strategy illustrated in [20]. Given an ini-
149 tial solution, the Serre-Green-Naghdi system is solved in two independent steps.
150 First, the elliptic equation (5c) is solved for the non-hydrostatic term ψ . Then,
151 an hyperbolic step is performed for equations (5a)-(5b), evolving the flow vari-
152 ables in time. This strategy solution has been shown to be very flexible and
153 robust, producing accurate results with different combinations of discretization
154 schemes in space and time. For this study, in the hyperbolic phase a third order
155 MUSCL finite volume scheme has been used, together with a third order SSP
156 Runge-Kutta method for the evolution in time. The elliptic phase is solved,
157 instead, with a classical second order finite element approach. The overall hy-
158 brid FV-FE scheme obtained is thus characterized by a dispersion error of the
159 same order, or smaller, than those produced by fourth order finite differencing,
160 providing that at least third order of accuracy is guaranteed for the hyperbolic
161 component. The interested reader can refer to [20] for more details.

162

163 *3.3. Boundary conditions*

164 The choice of the boundary conditions affects the flow field significantly [21].
165 While exact boundary conditions can be generally imposed in the case of homo-
166 geneous hyperbolic problems, this remains an active research topic when source
167 terms are included inside the equations. The task becomes even harder working
168 with dispersive models. Therefore, while the fully reflective wall boundary con-
169 dition can be obtained by imposing some symmetric conditions stemming from
170 the satisfaction of $\mathbf{u} \cdot \mathbf{n} = 0$ on the wall line (being \mathbf{n} the normal direction to
171 the wall), inflow and outflow boundaries require more complex treatments (*cf.*
172 [22, 23, 24, 25]).

173 In this work, the interest in long scale dynamics justifies the use of the NLSW
 174 invariants also when the SGN equations are solved inside the computational
 175 domain [26]. The illustrative results contained in section 5 show that the effects
 176 of this approximation on the large scale is completely negligible on both coarse
 177 and fine computational meshes.

178

179 In practice, the seaward boundary condition is applied by imposing in the
 180 incoming NLSW Riemann invariant the free surface given by the sea level tidal
 181 oscillation:

$$\zeta(t) = A_0 \sin\left(\frac{2\pi t}{T_0}\right) \quad (6)$$

182 We consider here the case of semi-diurnal tides with period $T_0 = 12.41$ [h].

183 On the landward boundary, the outflow condition is set imposing the informa-
 184 tion of still water (we recall that the river discharge is neglected at this level)
 185 coming from far on the right. However, the imposition of the homogeneous
 186 invariant cannot take into account the rise of the mean (tidally averaged) wa-
 187 ter level landward caused by the friction (*cf.* [5]), introducing a non-physical
 188 behavior of the solution in the outlet proximity. For this reason, the outflow
 189 boundary conditions has been coupled with an extension of the computational
 190 domain, to reduce the spurious influences on the solution in the region of study.
 191 In practice it has been enlarged up to $x = 6L_b$, to further limit non-physical
 192 effects due to the boundary condition.

193 In order to guarantee the reliability of the results, a sensitivity study has been
 194 performed in comparison with the technique of boundary imposition applied by
 195 [21] and a reference solution computed using a very long computational domain.
 196 For the interested reader the results of such study are reported in appendix B.

197 **4. Computations setting**

198 Tide propagation up to an estuary is, in nature, partly limited by an in-
 199 creasing bottom slope and by discharge. Considering that the effects of both
 200 the bathymetric variations and the river discharge have been, at first, neglected

201 in our simulations, even the weakest and linear tidal wave would be able to
 202 propagate landward and, being dissipated by only friction, it would reaches
 203 non-physical distances with also possible generation of unnatural bores. For
 204 this reason, and for later use, a characteristic physical length L_c has been intro-
 205 duced to limit the region in which the tidal signal is assumed to be physically
 206 relevant. In particular, examining real estuaries data, we observed that tidal
 207 bores occur, before reaching a distance of $3L_b$ from the estuary mouth, see table
 208 1. Thus, we have chosen to limit the region of interest for our simulations to
 $L_c = 3L_b$.

Estuaries	L_b [km]	x_c [km]	x_c/L_b
Gironde/Garonne	43	90	2.09
Hooghly	25	60	2.4
Humber	25	75	3.0
Pungue	17	50	2.94
Qiantang	40	90	2.25
Severn	41	55	1.34

Table 1: Ratio between the location of tidal bore inception x_c and convergence length L_b for some alluvial estuaries. Data taken from [3].

209
 210 Moreover, tidal bore inception is a continuous process which takes place as
 211 a gradual increase of the free surface slope at the beginning of the flood phase.
 212 The same continuous increase of steepness is observed in our simulations. A
 213 criterion is thus needed to detect the bore onset, within the domain $[0, L_c]$
 214 just defined. During the two measurement campaigns on the Garonne river,
 215 Bonneton et al.[3] observed that bore passage was associated to an increase in
 216 the value of the free surface spatial gradient, at the start of the flood, with at
 217 least one order of magnitude (from $\mathcal{O}(10^{-4})$ in the smooth case without tidal
 218 bore). For each numerical simulation we compute, in a post-processing phase,
 219 the spatial slope of the free surface all along the domain, up to L_c , retaining for
 220 each position x the maximum value in the tidal period. The quantity A_{max} has

221 been defined as:

$$A_{max} = \max_{x \in L_c} \left[\max_{t \in T_0} \left(\frac{\partial \zeta(x, t)}{\partial x} \right) \right] \quad (7)$$

222 and the following criterion to determine tidal bore onset is used: $A_{max} \geq 10^{-3}$.

223 5. Undular tidal bore formation

224 Preliminary simulations concerning the development of an undular tidal bore
225 into the idealized channel of figure 1 are reported in this section. We consider a
226 strongly nonlinear and weakly dissipative channel of $\epsilon_0 = 0.7$ and $\phi_0 = 10$. To
227 visualize the results we consider pointwise plots and distributions of the relevant
228 quantities along the channel axis. In developed flow conditions, deviations in
229 the transversal direction have been quantified to be less than 1.5%.

230

231 Figure 2 shows the time series over one tidal cycle of the computed free sur-
232 face elevation, measured at 11 gauges positions along the channel. It appears
233 evident that the results provided by the SGN model do not differ respect to
234 those obtained by using the NLSW model. Differences appear, instead, focus-
235 ing on the region of the shock formation. The results obtained are then reported
236 in figure 3 and show the formation process of a undular tidal bore. Also in this
237 case, the two models give identical results in the whole domain except when the
238 shock is formed (*cf.* top of figure 3). On the discontinuity, in fact, the SGN
239 model provides an undular bore with local formation of a train of secondary
240 waves. These waves are characterized by a wavelength of 50 [m] and a period of
241 6 [s] (*cf.* bottom of figure 3). However, it can be remarked that the position of
242 the bore inception, the mean bore jump and its celerity are well-described by
243 the NLSW model. This justifies its application for investigations on the large
244 scale estuary dynamics. Studies concerning the local effects on tidal bores or
245 flooding problems cannot, instead, avoid the use of a dispersive model to cor-
246 rectly reproduce the peaks of water height due to the secondary waves.

247 Field observations lead Bonneton *et al.* [3] to consider that the location of the
248 tidal bore onset is associated with the appearance of an inflexion point on the

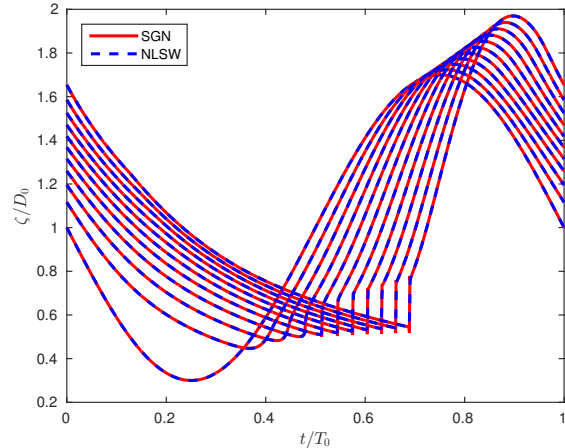


Figure 2: Illustrative result of a tidal propagation into an idealized channel with the shape described in section 2, $\epsilon_0 = 0.7$, $\phi_0 = 10$. Computed free surface profile, measured at 11 stations along the channel corresponding to $x = \alpha L_B$ with $\alpha = 0 : 1/3 : 3$. The simulation have been realized using both the NLSW and the SGN models.

249 tidal wave profile. However, these authors stress the difficulty to characterize
 250 the tidal bore onset on the river, since this would require a high density of water
 251 elevation measurements over a long distance. By contrast, with our numerical
 252 simulations we are able to provide a full set of subsequent snapshots (*cf.* figure
 253 4), describing the progressive transition from a tidal wave regime without bore
 254 (*cf.* figures 4a and 4b) to a well-developed undular tidal bore regime (*cf.* fig-
 255 ures 4g and 4h). The gradual evolution of the surface profile towards the bore
 256 inception passes by the appearance of an inflexion point at the beginning of the
 257 rising tide.

258 In the middle and upper part of the estuary, the value of A_{max} , used in our
 259 tidal bore onset criterion, is registered at the beginning of the rising tide. As
 260 a consequence, the pictures of figure 4 allow to observe the temporal evolution
 261 of such quantity as the tide propagates landward. The values of $\max_{x \in L_c} \left(\frac{\partial \zeta}{\partial x} \right)$ for
 262 the eight pictures of figure 4 are, thus, showed in table 2 for the two NLSW and
 263 SGN model. It is worth to note that the dispersive terms becomes relevant after
 264 the threshold of A_{max} has been reached, *i.e.* when tidal bore occurrence has

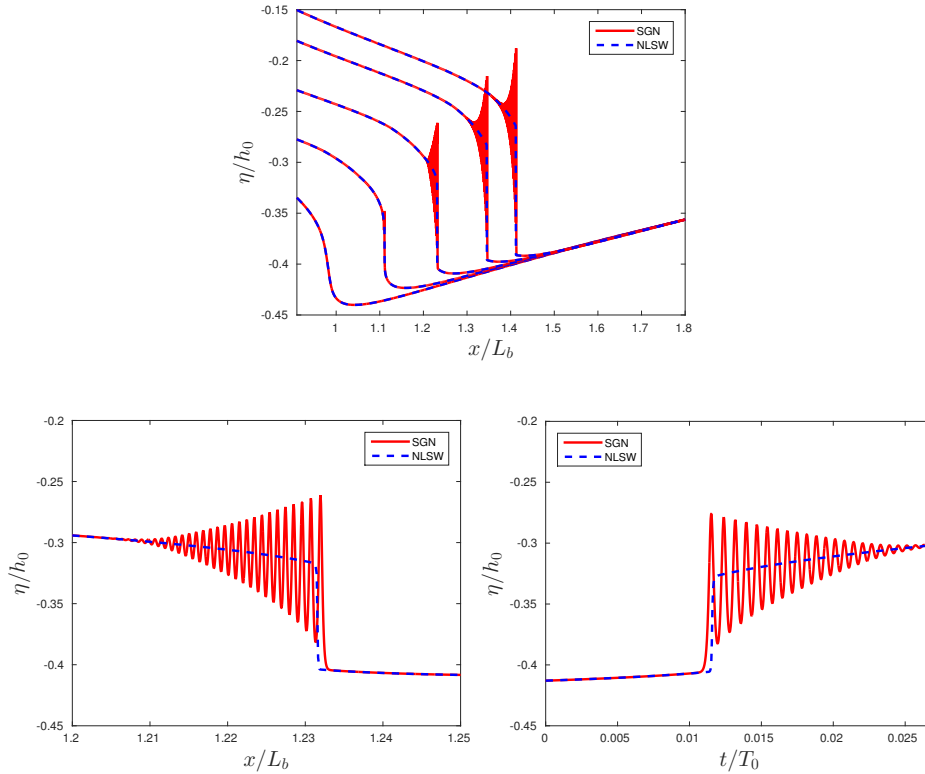


Figure 3: Illustrative result of tidal propagation into an idealized channel with the shape described in section 2, $\epsilon_0 = 0.7$, $\phi_0 = 10$. Top: computed free surface profile at different increasing times of the simulation. Bottom-left: free surface signal in space. Bottom-right: free surface signal in time.

265 already been flagged by our criterion. We can, thus, conclude that tidal bore
 266 appearance is completely determined by the values of the external parameters
 267 ϵ_0 , δ_0 and ϕ_0 and is not influenced by the choice of the model used for the
 268 numerical simulations.

269 6. Study of tidal bore occurrence

270 The results of the previous section show that dispersive effects are not neces-
 271 sary to study the large scales of the propagation and transformation of the tide.
 272 At these scales the NLSW system is a sufficiently accurate and more efficient

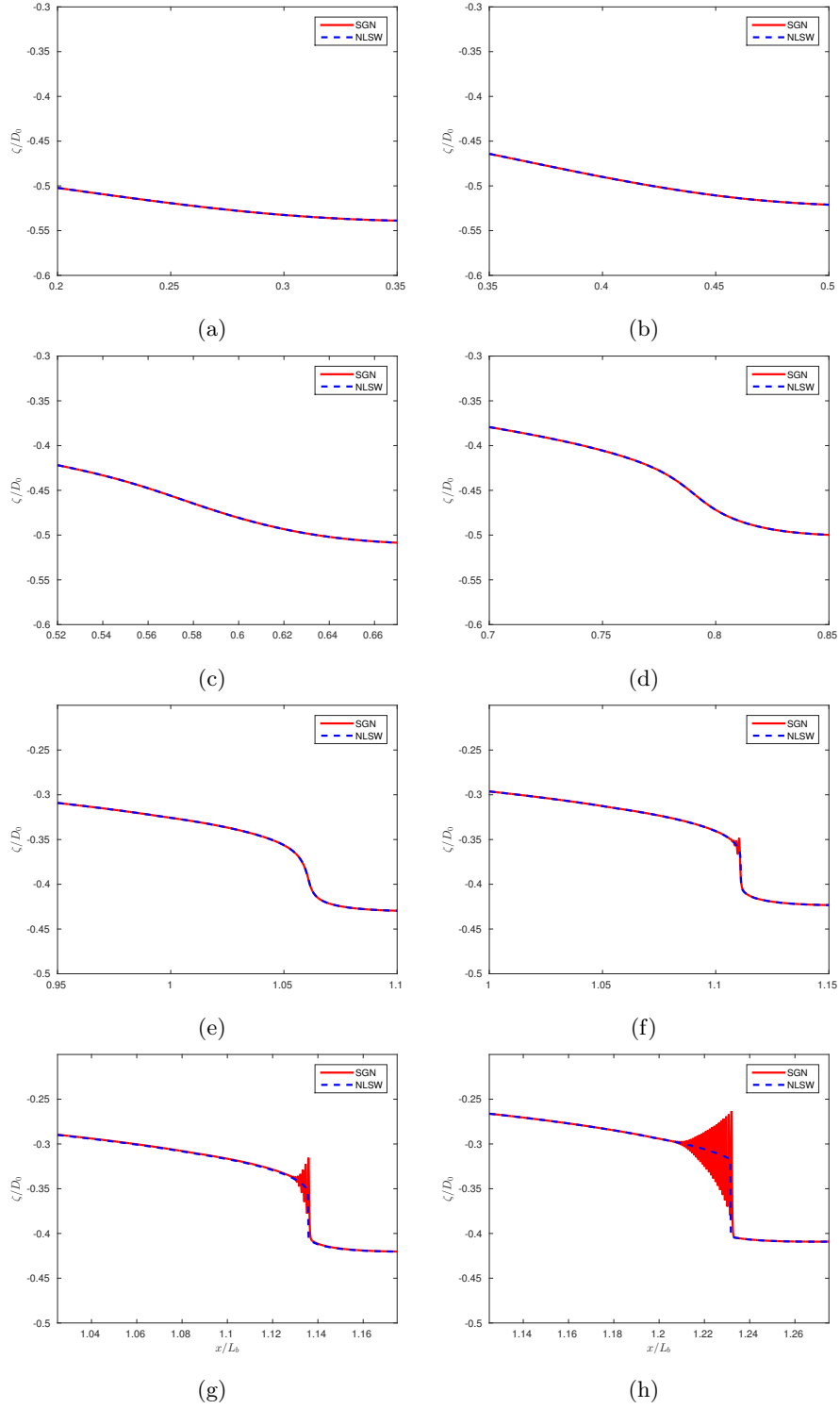


Figure 4: Computed free surface profile at different increasing times of the simulation, showing the undular bore inception from the formation of an inflexion point of the wave profile: from top left to bottom right.

	NLSW	SGN
a)	7.25×10^{-5}	7.25×10^{-5}
b)	1.05×10^{-4}	1.05×10^{-4}
c)	$1,74 \times 10^{-4}$	$1,74 \times 10^{-4}$
d)	4.11×10^{-4}	4.11×10^{-4}
e)	1.9×10^{-3}	1.9×10^{-3}
f)	2.87×10^{-3}	1.61×10^{-3}
g)	5.04×10^{-3}	3.77×10^{-3}
h)	9.47×10^{-3}	7.38×10^{-3}

Table 2: Values assumed by the quantity $\max_{x \in L_c} \left(\frac{\partial \zeta}{\partial x} \right)$ in the several pictures of figure 4 and for the two NLSW and SGN models. Bold numbers represent values which satisfy the tidal bore onset criterion: $A_{max} \geq 10^{-3}$

273 model. This is why we will employ it here to perform the numerical investiga-
274 tion of the space (ϕ_0, ϵ_0) of dimensionless parameters, trying to quantify the
275 favorable conditions for bore inception. However, dispersion simulations will
276 still be used in some cases to provide some quantification of the local order of
277 magnitude of the non hydrostatic terms. This quantitative comparison will al-
278 low to comfort our hypothesis and provide further insight into the mechanisms
279 of bore formation.

280

281 6.1. Investigation of the plane (ϕ_0, ϵ_0)

282 We have performed 225 simulations of the idealized case of study defined
283 in section 2, corresponding to an equivalent number of estuaries. We recall
284 that the value of convergence ratio is constant, $\delta_0 = 2$, and thus each simula-
285 tion represents a unique combination of the parameters ϵ_0, ϕ_0 , corresponding to
286 precise conditions of the tidal forcing at the mouth and to specific geometrical
287 and physical properties of the channel. In such a way we have systematically
288 investigated the plane (ϕ_0, ϵ_0) , applying the criterion described in section 4 in

289 order to detect bore formation. Figure 5(left) shows the contour lines of the
 290 quantity A_{max} in the plane of the parameters (ϕ_0, ϵ_0) , performed by collecting
 291 and linearly interpolating the simulations' results. The red color denotes the re-
 292 gion where the bore detection criterion is satisfied, while the blue one represents
 293 cases characterized by a smooth solution. Figure 5(right) will be discussed later
 294 on. The results show that there exists a critical curve $\epsilon_c(\phi_0)$ that can be traced
 295 in this plane, dividing tidal-bore and no-tidal-bore estuaries. This curve is the
 white dashed line traced in figure 5(left). Observing the shape of the isolines

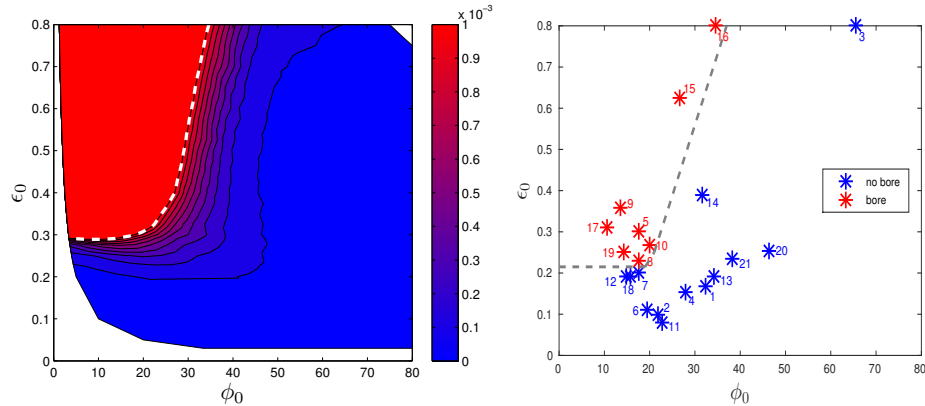


Figure 5: (Left): Isocurves of the quantity A_{max} in the plane of the parameters (ϕ_0, ϵ_0) , the white dashed line represents the $\epsilon_c(\phi_0)$ curve, namely the limit for tidal bore appearance following the criterion $A_{max} \geq 10^{-3}$. (Right) : Projection of real alluvial estuaries data on the plane (ϕ_0, ϵ_0) ; with a grey dashed line (- -) we have represented by hand the transition between the two regimes, inspired by the similar trend in the left picture. The database used to generate the picture can be found in table 2 of [13], for brevity and completeness we list here the name and number of the estuaries included in the picture: 1. Chao Phya; 2. Columbia; 3. Conwy; 4. Corantijn; 5. Daly; 6. Delaware; 7. Elbe; 8. Gironde; 9. Hooghly; 10. Humber; 11. Limpopo; 12. Loire; 13. Mae Klong; 14. Maputo; 15. Ord; 16. Pungue; 17. Qiantang; 18. Scheldt; 19. Severn; 20. Tha Chin; 21. Thames. Sources: [6] for estuaries 1, 4, 11, 13, 14, 18, 20; [1] for 2, 3, 6, 7, 15, 19, 21; [3] for 8, 9, 10, 16, 17; [27] for 5; [28] for 12.

296

297 in figure 5(left), two different behaviors can be distinguished, depending on the
 298 values assumed by the friction parameter ϕ_0 .

299 The first region is characterized by values of the friction parameter in the

300 range $1 < \phi_0 \leq \sim 20$. Here the mechanism of bore inception appears to be fully
 301 controlled by the nonlinear parameter ϵ_0 . Figure 6 shows a comparison between
 302 two numerical results computed using two different values of ϵ_0 , one just above
 303 the critical curve and one just below it ($\epsilon_0 = 0.3$ and $\epsilon_0 = 0.225$ respectively),
 304 at a constant value of ϕ_0 equal to 13.33. The comparison is made in terms of
 305 the free surface and velocity time series, respectively in figure 6(a) and 6(b),
 306 measured at the location $x = L_c$. In both figures, the signals associated to the
 307 case at higher ϵ_0 are characterized by a greater distortion at the beginning of
 308 the flood phase, leading to bore formation according to our threshold. The two
 309 zooms, displayed in figures 6(c) and (d), allow to better appreciate the different
 310 time gradients exhibited by the water wave on the time scale of the tidal bore
 311 (around 20 minutes). It is also interesting to note that the free surface profile
 312 of figure 6(a) does not display a Burger's like shock, but rather a *knee* shape
 313 is observed. This is mainly due to the fact that the nonlinear effect of friction
 314 prevails on the advective one, remaining the dominant nonlinearity for the major
 315 part of the wave transformation. Figure 7 displays the relative importance of
 316 the various terms in the momentum equation during a tidal cycle in the previous
 317 case of bore development ($\epsilon_0 = 0.3$ and $\phi_0 = 13.33$). In the figures, the time
 318 evolution of these quantities is represented at three equispaced locations along
 319 the channel, in particular at $x = \frac{1}{3}L_c$, $x = \frac{2}{3}L_c$ and $x = L_c$. It emerges that
 320 the advective term remains negligible in the momentum equation and the bore
 321 formation results from a balance between acceleration, friction and hydrostatic
 322 terms. Only in the presence of incipient bore, the relative importance of the
 323 advective term rises up overcoming the frictional nonlinearity. This behaviour
 324 can be also recovered when a dispersive bore development is simulated. For
 325 the previous case of undular bore formation of section 5, the time variations
 326 of the relative magnitude for the momentum equation's terms are compared
 327 in figure 8. For sake of clarity, data are shown for the small time of the bore
 328 passage at two space locations: just before (left) and after (center and right)
 329 the appearance of the secondary waves. It can be seen that, as in the previous
 330 case of figure 7, the advective term becomes the relevant nonlinear term on the

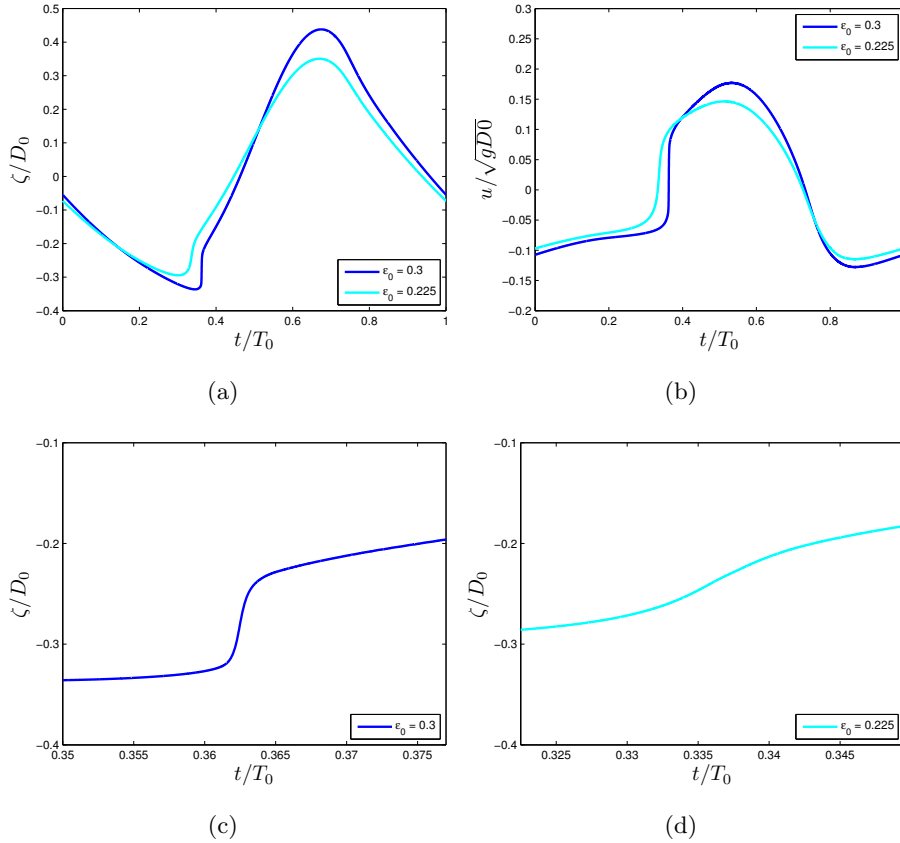


Figure 6: Time variation of the free surface elevation (a) and the velocity (b) signals measured at $x = L_c$ for a fixed value of $\phi_0 = 13.33$ and the two different values of $\epsilon_0 = 0.225$ (–) and $\epsilon_0 = 0.3$ (–). (c) and (d) are two zooms on the water wave profile at the beginning of the flood phase, on the time scale of the tidal bore (around 20 minutes).

331 bore location. However, in this case, its increase is partially limited by the rise
 332 of the dispersive term in a general context dominated by the balance between
 333 the inertial and the hydrostatic contributions.

334

335 For higher values of ϕ_0 ($\phi_0 \geq \sim 20$), the isolines of A_{max} spread out form-
 336 ing a wider transition region but, more important, display an almost vertical
 337 slope. This implies an increasing role of the friction parameter in the physical
 338 mechanism of bore formation. In figure 9, we show the solutions computed for

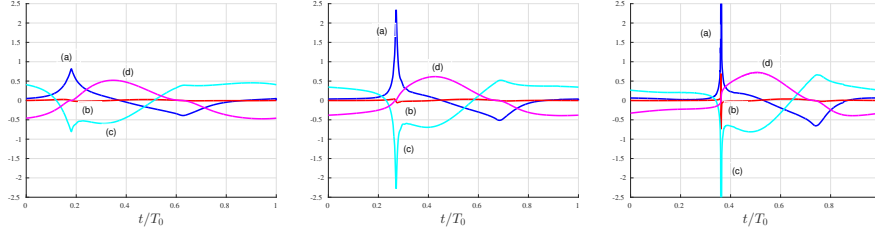


Figure 7: The order of magnitude of the several dimensionless terms in the momentum equation of system (17) without dispersion; three test sections are presented: at $x = \frac{1}{3} L_c$ (left), $x = \frac{2}{3} L_c$ (center) and $x = L_c$ (right): (a) $\frac{\partial \mathbf{u}}{\partial t}$, (b) $\frac{K}{L} \epsilon_0 (\mathbf{u} \cdot \nabla) \mathbf{u}$, (c) $\frac{1}{K L} \delta_0^2 \nabla \zeta$ and (d) $K \frac{\epsilon_0 \phi_0}{\delta_0} \frac{\mathbf{u} |\mathbf{u}|}{D}$. Upper and lower peaks on the figure (right) reach values respectively of 30.65 and -28.61 .

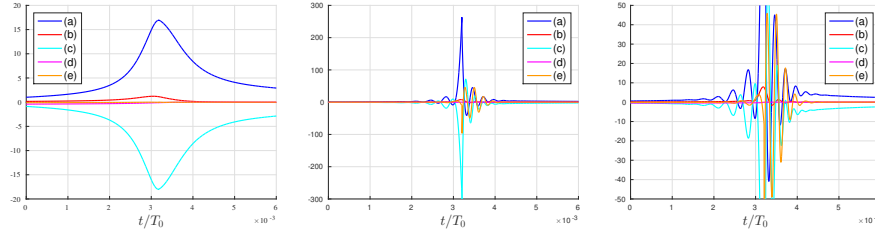


Figure 8: The order of magnitude of the several dimensionless terms in the momentum equation of system (17), including the dispersion; two test sections are presented: at $x = \frac{1.02}{3} L_c$ (left) and $x = \frac{1.12}{3} L_c$ (center), focusing on the time scale of the bore passage, while the third picture (right) represents, for clearness, a zoom of the central one: (a) $\frac{\partial \mathbf{u}}{\partial t}$, (b) $\frac{K}{L} \epsilon_0 (\mathbf{u} \cdot \nabla) \mathbf{u}$, (c) $\frac{1}{K L} \delta_0^2 \nabla \zeta$ and (d) $K \frac{\epsilon_0 \phi_0}{\delta_0} \frac{\mathbf{u} |\mathbf{u}|}{D}$ and (e) $\mu^2 \Psi$.

339 two cases across the transition zone ($\phi_0 = 20$ and $\phi_0 = 40$ respectively), keep-
 340 ing constant $\epsilon_0 = 0.4$. Once again, we look to the free surface and velocity
 341 time signals to compare the two results, figures 9(a) and 9(b) respectively. It
 342 clearly appears that an increase of the value of the friction parameter ϕ_0 is
 343 directly associated to both potential and kinetic energy dissipation, leading to
 344 more damped profiles. This process decreases the local nonlinearity of the wave
 345 which, in turn, is smeared out, as one can see from the free surface zooms on the
 346 time scale of the bore (figures 9(c) and 9(d)). Moreover, figures 9(b) displays
 347 the particular tendency of the tidal current to become constant during the ebb
 348 tide for large values of the friction parameter (strongly dissipative estuaries), in

349 agreement with previous studies (e.g. [1] and [3]).

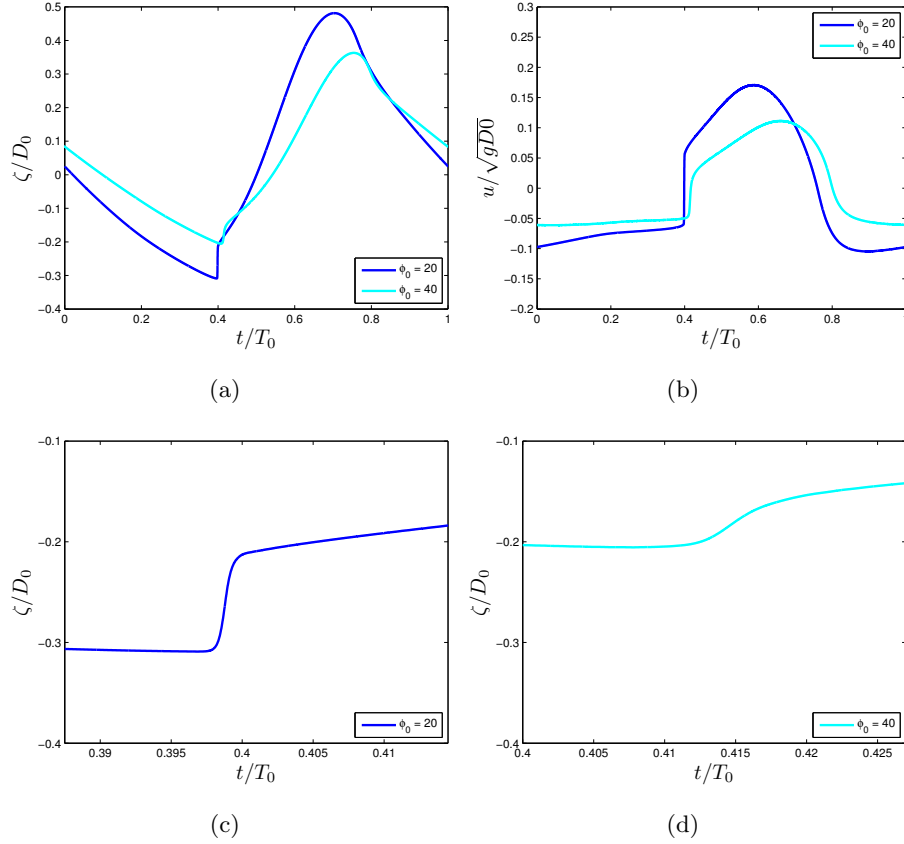


Figure 9: Time variation of the free surface elevation (a) and the velocity (b) signals measured at $x = L_c$ for a fixed value of $\epsilon_0 = 0.4$ and the two different values of $\phi_0 = 20$ (—) and $\phi_0 = 40$ (—). (c) and (d) are two zooms on the water wave profile at the beginning of the flood phase, on the time scale of the tidal bore (around 20 minutes).

350 We can schematically summarize that the nonlinear parameter ϵ_0 mainly
 351 relates to the distortion mechanism which leads to bore formation, while the
 352 friction parameter ϕ_0 mainly relates the dissipation of the tidal wave, unfavor-
 353 able to bore generation.

354 The separation between estuaries displaying or not a tidal bore, which emerges
 355 from our numerical results, is in qualitative agreement with real-estuary obser-
 356 vations analyzed in [13]. A list of tidal and geometrical properties for 21 conver-

357 gent alluvial estuaries (8 of them displaying a bore and 13 not) has been used in
 358 [13] to produce figure 5(right), reported here for sake of clarity. In the picture, a
 359 grey dashed line dividing tidal-bore and no-tidal-bore estuaries has been traced
 360 by hand, inspired by the trend of the critical curve emerged in figure 5(left).
 361 We can notice that the numerical critical curve $\epsilon_c(\phi_0)$ and the data-based one
 362 only slightly differ considering the several simplifying modeling assumptions.
 363 In particular, in real alluvial estuaries the general decrease of depth landward
 364 is favorable to bore inception and this can cause the critical data-based curve
 365 (figure 2b of [13]) to be located slightly below with respect to the modeling one
 366 on figure 5(left).

367 From the observations made in the previous paragraph, a close relation be-
 368 tween bore formation and tidal damping emerges. A standard parameter used
 369 in the literature [29, 30] to measure the amplification/damping of the tidal wave
 370 during its propagation along the estuary is the rate of change of the tidal range
 371 Tr , defined in accordance to reference [30] as:

$$\delta_{\text{Tr}} = \frac{1}{\text{Tr}} \frac{d\text{Tr}}{dx} . \quad (8)$$

372 In the present work we integrate equation (8), from the estuary mouth to $x = L_c$
 373 (end of our region of study), and we compute, for each simulation performed,
 374 the quantity:

$$\Delta_{\text{Tr}} = \frac{\text{Tr}(L_c) - \text{Tr}(0)}{\text{Tr}(0)} \quad (9)$$

375 using the tidal range at the estuary mouth $\text{Tr}(0)$ as a scaling factor.

376 Figure 10(left) shows, on the same plane (ϕ_0, ϵ_0) of figure 5, the contour lines
 377 of the computed quantity Δ_{Tr} , obtained by linearly interpolating the values of
 378 each simulation. The black dashed line is the contour line for $\Delta_{\text{Tr}} = 0$, namely
 379 the marginal curve for tidal range amplification, where all the estuaries with
 380 unamplified and undamped wave lie. It represents an ideal situation for which
 381 the amplification effect associated to funneling is exactly balanced by friction.
 382 The marginal curve divides the plane into two regions; estuaries located below
 383 are characterized by a tidal range amplification while estuaries located above
 384 are affected by damping. A simple analytical model, derived by Savenije et al.

385 [29] in the linearized case, allows to explicitly compute the damping factor of
 386 an estuary as a function of the three external independent parameters of the
 387 estuarine dynamics. According to this model, Toffolon et al. [2] found that
 388 synchronous estuaries ($\delta_{Tr} = 0$) lie on a curve, which can be recast in terms of
 389 our parameters as:

$$\epsilon_0 = \frac{\delta_0(\delta_0^2 + 1)}{\phi_0} . \quad (10)$$

390 Using the value of $\delta_0 = 2$ in (10), we get the red curve plotted in figure 10(left).
 391 A good agreement is observed between the marginal curve obtained through
 392 numerical simulations (black dashed line) and the one of the analytical model
 393 of Savenije (red line), especially for low values of ϵ_0 , namely the linear regime.

394 From figure 10(left) it is interesting to note that ϵ_0 plays a fundamental role
 395 also in the damping/amplification process. If we fix the physical and geometrical
 396 properties L_b , C_{f0} , D_0 , this corresponds to a specific estuary configuration
 397 with ϕ_0 constant in addition to $\delta_0 = 2$. In this context, the variations of
 398 ϵ_0 can be considered as associated with neap-spring tide cycles. We can, thus,
 399 conclude that strong tides lead to weaker tidal wave amplification values and, for
 400 particularly strong tides, the wave most likely will be damped. This result is in
 401 qualitative agreement with the physical observation made in [3] for the Garonne
 402 river. Their measurements showed that, for such estuary always characterized
 403 by tidal wave amplification, minor amplifications were related to higher values
 404 of ϵ_0 , observed during spring tides.

405 The superimposition of the computed marginal curve on the contour lines of
 406 the quantity A_{max} , in figure 10(right), shows that a large part of the red region
 407 in the figure, lies in the part of the plane (ϕ_0, ϵ_0) characterized by damping of
 408 the tidal range. This means that, despite a reduction of the local nonlinearity of
 409 the wave, this remains high enough to develop distorted profiles and to produce
 410 bores. We can conclude that, contrary to what is generally accepted, tidal
 411 range amplification along the estuary is not a necessary condition for tidal bore
 412 formation.

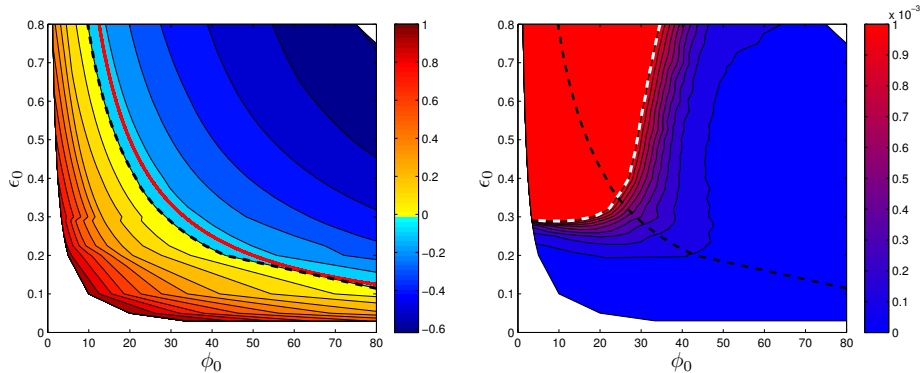


Figure 10: (Left): contour lines of the quantity Δ_{Tr} on the plane (ϕ_0, ϵ_0) ; the black dashed line (- -) represents the marginal curve resulting from the computations, while the continuous red one (-) is the analytical marginal curve of the Savenije model [30]. Hot colors cover the region of amplification of the tidal wave during propagation; cold colors represent damping. (Right): the computed marginal curve (- -) is superimposed on the A_{max} contour lines.

413 7. Influence of river discharge

414 In the previous sections, we have analyzed tidal wave transformation and
 415 tidal bore occurrence in a simplified context in which freshwater river discharge
 416 was neglected. However, it is well known that tide in estuaries may be signif-
 417 icantly affected by the rate of discharge [16, 5]. The effects of river discharge
 418 become much more important moving landward from the mouth of the estuary
 419 and can influence for bore formation. The present section will provide a qual-
 420 itative estimation on the effects of discharge, leaving a full quantitative study
 421 for future works.

422 In the experimental campaigns on the Garonne river, Bonneton et al. [3]
 423 observed that small river discharges Q were favorable to tidal range amplifi-
 424 cation and bore occurrence, while significant freshwater discharges offsets the
 425 amplification mechanism related to estuary convergence. Horrevoets et al. [16]
 426 described, with an analytical model, that the influence of river discharge on tidal
 427 damping takes place mainly through friction. Generally speaking, the tidally
 428 averaged free surface elevation along the estuary does not coincide with the
 429 mean sea level, due to the nonlinear frictional effect on the averaged water level

430 $\bar{D}(x)$. In practice there is a monotone increase of $\bar{D}(x)$ landward, proportional
 431 to the river discharge Q , see [31, 5]. Moreover, a damping of the local tidal
 432 range $Tr(x)$ has been pointed out by Bonneton et al. [3], hence the local non-
 433 linear parameter $\epsilon(x) = Tr(x)/(2\bar{D}(x))$ is a decreasing function of Q . Due to
 434 this damping effect, tidal bores are rarely observed for strong freshwater river
 435 discharges.

436 For a fixed estuary (fixed δ_0 and ϕ_0), the dimensionless parameters governing
 437 the flow dynamics are the amplitude of tidal forcing ϵ_0 and the dimensionless
 438 intensity of river discharge Q_0 . The goal of the present section is to explore the
 439 space of parameters (ϵ_0, Q_0) in order to find, for an estuary characterized by
 440 $\delta_0 = 2$ and $\phi_0 = 18$ (values closed to the ones of the Garonne river), a critical
 441 curve $\epsilon_c(Q_0)$ for tidal bore development, following the criterion $A_{max} \geq 10^{-3}$.
 442 In order to perform our investigation, we have to express Q_0 as a function of the
 443 external variables of the problem. The scaling analysis proposed in [13] leads
 444 to the definition of a parameter $K = \frac{U_0 D_0}{A_0 \omega_0 L_b}$ (see also appendix A for details),
 445 that has been measured to be $K \sim 1$ in convergent alluvial estuaries [3]. A
 446 characteristic velocity scale $U_0 = \epsilon_0 \omega_0 L_b$ can, thus, be derived. Being B_0 the
 447 width at the estuary mouth (figure 1), we finally define:

$$Q_0 = \frac{Q}{A_0 B_0 L_b \omega_0} . \quad (11)$$

448 The river discharge is introduced by the boundary condition already described in
 449 section 3, through the incoming Riemann invariant from far on the right. Figures
 450 11 shows, for the particular estuary considered, the effect of an increasing river
 451 flow in terms of normalized free surface elevation and velocity signals at the
 452 position $x = L_c$ along the channel. The simulations were performed using
 453 $\epsilon_0 = 0.32$ and a range of values $Q_0 \in [0, 4.16 \times 10^{-3}]$, obtained by scaling
 454 the typical values of the Garonne river through relation (11). In particular,
 455 the values $Q_0 = 4.16 \times 10^{-4}$ and $Q_0 = 4.16 \times 10^{-3}$ correspond to the low and
 456 high characteristic fresh water discharges measured in the Garonne (respectively
 457 $Q = 150 [m^3/s]$ and $Q = 1500 [m^3/s]$). In figure 11 (a), we observe that the
 458 dimensionless mean water depth $\bar{D}(L_c)/D_0$ increases with Q_0 , from 1.033 with

459 $Q_0 = 0$ to 1.219 with $Q_0 = 4.16 \times 10^{-3}$. We can also measure the damping
 460 effect of freshwater river discharge on the tidal range; the dimensionless value
 461 $\Delta_{Tr}(L_c)$ (as defined in (8)) goes from 0.156 with $Q_0 = 0$ (amplified case) to
 462 -0.041 with $Q_0 = 4.16 \times 10^{-3}$ (damped case). An important vertical shift of
 463 the velocity curve, in agreement with field observations [16], can be observed in
 464 figure 11 (b), moving towards the condition of unidirectional flow. Moreover,
 465 it can be noticed that this result confirms the theoretical predictions set by
 466 Horrevoets et al. [16] concerning the evolution of the phase lag between high
 467 water and high water slack (and at the same time between low water and low
 468 water slack). Note that all the effects described are small below the value of
 469 $Q_0 = 4.16 \times 10^{-4}$ and the discharge does not affect the topology of the tidal
 470 wave for the river flow values typically observed in the Garonne river at the end
 471 of the summer season. Thus, the parametric analysis performed in section 2, by
 472 neglecting Q_0 , can be considered valid in this range of small Q_0 .

473 In figure 11 (c), the zoom on the time scale of the bore displays the ten-
 474 dency of the free surface profile to become much smoother as the value of river
 475 discharge increases. In order to explore better this point, we have performed 47
 476 simulations for different combinations of tidal amplitude and river discharge (ϵ_0 ,
 477 Q_0). The values of A_{max} , obtained for all the simulations, have been plotted in
 478 figure 12. Note that we chose to represent in the y -axis of the figure the product
 479 $Q_0\epsilon_0$, rather than simply Q_0 , in order to remove the dependence of Q_0 from A_0
 480 (11). The figure shows that, in the presence of weak river discharges, estuarine
 481 dynamics is not influenced by Q_0 and, consequently, the effects of discharge can
 482 be considered negligible in the bore formation process. A qualitative critical
 483 curve $\epsilon_c(Q_0)$ has been traced by hand (grey dashed line in figure 12) according
 484 to the few computations performed and following the criterion $A_{max} \geq 10^{-3}$.
 485 This trend is in qualitative agreement with experimental data for the Garonne
 486 river, presented in [13].

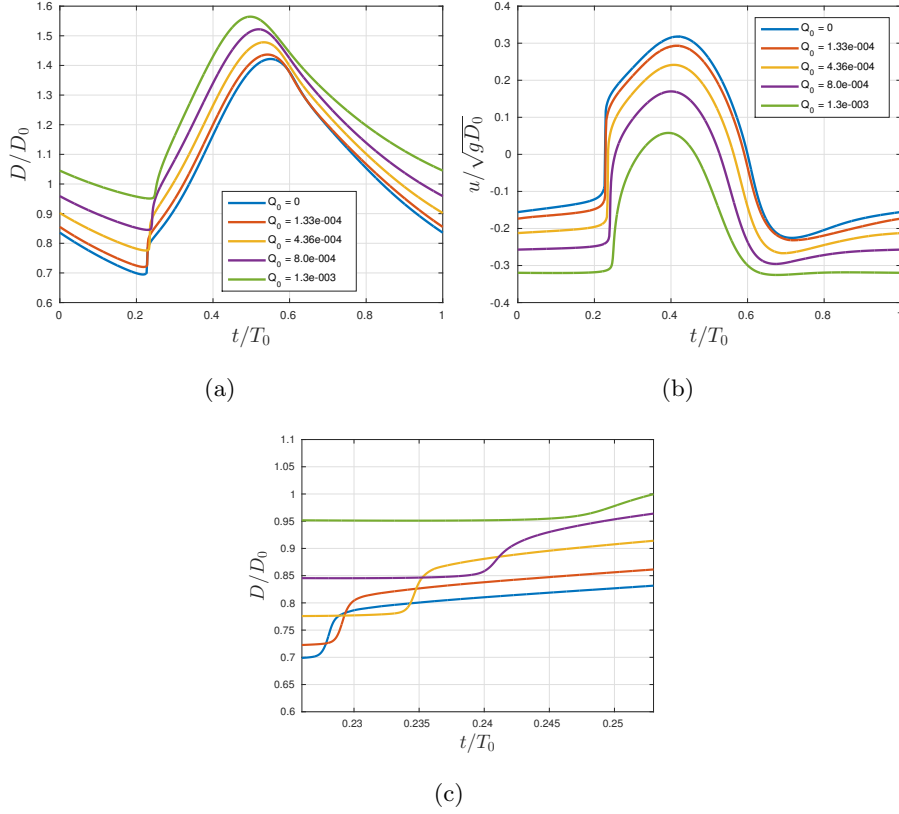


Figure 11: Time variation of the water depth (a) and velocity (b) signals measured at $x = 3L_b$ for an ideal estuary characterized by $\epsilon_0 = 0.32$, $\phi_0 = 18$ and increasing values of freshwater discharge from $Q_0 = 0$ to $Q_0 = 4.16 \times 10^{-3}$ (in particular the values have been chosen considering the typical range of values displayed by the Garonne river and measured by Bonneton et al. [3]). Figure (c) represents a zoom on (a) in the time scale of the bore (around 20 min).

487 8. Conclusions

488 The two-dimensional Serre-Green-Naghdi system of equations has been used
 489 in order to simulate the inception of tidal bores in convergent alluvial estuaries
 490 of idealized geometry. Exploiting the dispersive properties of the model, we
 491 were, thus, the first to reproduce the formation of an undular tidal bore inside a
 492 channel, to the authors' knowledge. The results obtained have illustrated that
 493 dispersion does not impact the large scale of propagation of the tide, as it comes

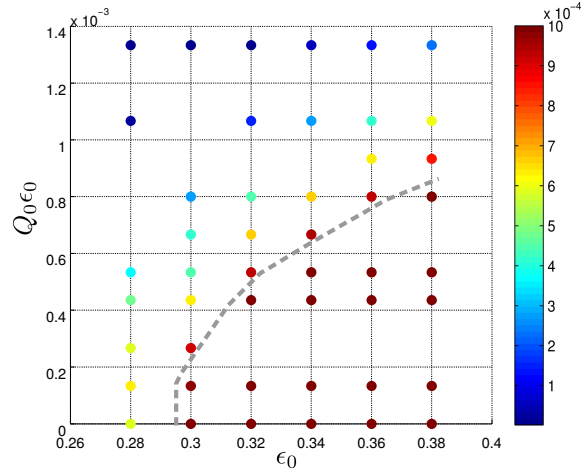


Figure 12: Circles represent computations performed for a fixed estuary ($\delta_0 = 2$ and $\phi_0 = 18$) varying the values of the tidal forcing amplitude A_0 and river discharge Q_0 ; colors represent the intensity of A_{max} for each computation; with a grey dashed line we have represented by hand the $\epsilon_c(Q_0)$ curve, namely the limit for tidal bore appearance following the criterion $A_{max} \geq 10^{-3}$

494 also from the scaling analysis of the equations proposed in appendix A, and af-
 495 fects the solution only in the proximity of bore formation. For these reasons,
 496 an accurate description of the free surface profile at large scale can be obtained
 497 via the simpler NLSW system. Under the hypotheses of constant bathymetry
 498 and negligible river discharge, we have thus employed the NLSW equations to
 499 numerically investigate the bore occurrence in convergent alluvial estuaries of
 500 idealized geometry.

501 The scaling of the equations shows that estuarine dynamics is fully controlled
 502 by three dimensionless parameters entirely dependent on the estuary geometri-
 503 cal properties and tidal forcing: the nonlinearity ϵ_0 , the convergence parameter
 504 δ_0 and the friction parameter ϕ_0 , defined by (3). Taking a constant value of
 505 $\delta_0 = 2$, we have numerically explored the space (ϕ_0, ϵ_0) . By means of a bore
 506 detection criterion, we have traced the critical line $\epsilon_c(\phi_0)$ dividing estuaries into
 507 displaying or not a tidal bore. This curve is in good agreement with real es-
 508 tuaries data, despite the several assumptions made, and provides the necessary

509 conditions for tidal bore formation. These conditions are a result of a complex
 510 equilibrium between nonlinear distortion and tidal range damping/amplification
 511 processes both driven by the dissipation parameter $D_i^* \propto \epsilon_0 \phi_0$ multiplying the
 512 friction, the dominant nonlinear term for this class of estuaries. The particular
 513 shape of $\epsilon_c(\phi_0)$ shows that, for low values of ϕ_0 (indicatively $1 < \phi_0 \leq \sim 20$),
 514 bore formation depends almost exclusively on the nonlinear parameter ϵ_0 , while
 515 being, instead, mainly disciplined by the dissipation, related to the value of ϕ_0 ,
 516 for $\phi_0 \geq \sim 20$.

The critical curve intersects the computed marginal curve of amplification, di-

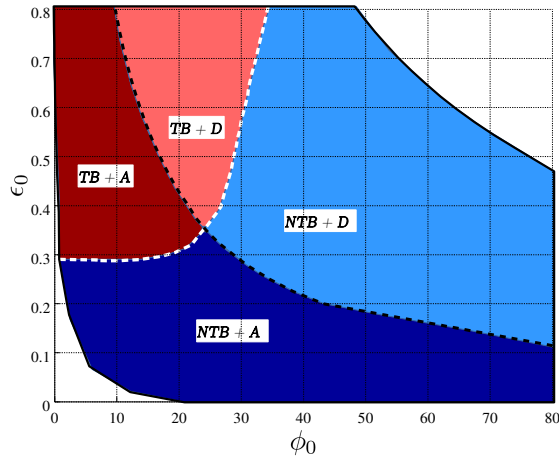


Figure 13: The computed critical line for bore formation (white dashed line) and the computed marginal curve of amplification (black dashed line) divide the (ϕ_0, ϵ_0) plane into four main areas. In the picture, TB stands for tidal-bore estuaries, while NTB stands for no tidal-bore estuaries; A indicates amplification of the tidal wave along the estuary, D damping.

517
 518 viding the plane into four main areas. Estuaries will thus experience tidal range
 519 amplification or damping, tidal bore formation or not, depending on which re-
 520 gion in the plane they belong to (see figure 13). The existence of a sector
 521 characterized by tidal bore generation and tidal range damping shows that tidal
 522 range amplification along the estuary is not a necessary condition for tidal bore
 523 occurrence, as it is instead commonly assumed in the literature [32]. This result
 524 is also in agreement with field observations analyzed in [13].

525 Finally, we have studied the effect of river discharge for estuaries character-
 526 ized by $\delta_0 = 2$ and $\phi_0 = 18$ (which are close to the values displayed by
 527 the Gironde/Garonne estuary). We have shown that for low Q_0 (i.e. $Q_0 <$
 528 4.16×10^{-3}), corresponding to the dry season, the effect of river discharge on
 529 tidal wave dynamics and bore formation can be neglected.

530

531 The above findings are based on several simplifying assumptions, that have
 532 allowed a clear understanding of the bore inception mechanism. Other effects
 533 influencing the spatial location of bore development have been so far ignored
 534 and may arise due to the variable bathymetry, river banks and meanders. The
 535 consideration of such effects will require significant attention, but will provide
 536 a more thorough comprehension when approaching the analysis of real natural
 537 estuaries.

538 Appendix A: Scaling of the SGN equations

539 In this section we report some details concerning the application of the scal-
 540 ing proposed in [13] to the SGN system of equations (5). The following scaling
 541 of the physical variables is thus applied:

$$\begin{aligned} x = L_0 x' ; \quad y = L_0 y' ; \quad t = \frac{t'}{\omega_0} ; \quad D = D_0 D' ; \quad (12) \\ \zeta = A_0 \zeta' ; \quad \mathbf{u} = U_0 \mathbf{u}' . \end{aligned}$$

542 The governing equations (5a) and (5b), written in dimensionless form, will thus
 543 read (dropping the primes for sake of clarity):

$$\frac{\partial \zeta}{\partial t} + \frac{K}{\mathcal{L}} (\epsilon_0 \mathbf{u} \cdot \nabla \zeta + D \nabla \cdot \mathbf{u}) = 0 , \quad (13a)$$

$$\frac{\partial \mathbf{u}}{\partial t} + \frac{K}{\mathcal{L}} \epsilon_0 (\mathbf{u} \cdot \nabla) \mathbf{u} + \frac{1}{K \mathcal{L}} \delta_0^2 \nabla \zeta + K \frac{\epsilon_0 \phi_0}{\delta_0} \frac{\mathbf{u} |\mathbf{u}|}{D} = \boldsymbol{\psi} . \quad (13b)$$

544 where $\mathcal{L} = \frac{L_0}{L_b}$ and $K = \frac{U_0 D_0}{A_0 \omega_0 L_b}$ are functions of the length and velocity scales
 545 of the phenomenon [13] and the scale factor $\frac{2\pi U_0}{T_0}$ has been used for the non-
 546 hydrostatic term $\boldsymbol{\psi}$.

547 Considering a flat bathymetry, the linear operators $\mathbb{T}(\mathbf{w})$ and $\mathbb{Q}(\mathbf{w})$, applied to
 548 a generic vector \mathbf{w} , are:

$$\mathbb{T}(\mathbf{w}) = -\frac{1}{3D} \nabla \left(D^3 \nabla \cdot \mathbf{w} \right), \quad (14a)$$

$$\mathbb{Q}(\mathbf{w}) = \frac{2}{3D} \nabla \left[D^3 \left(\nabla \mathbf{w}_1 \cdot \nabla^\perp \mathbf{w}_2 + (\nabla \cdot \mathbf{w})^2 \right) \right]; \quad (14b)$$

549 in which \mathbf{w}_1 and \mathbf{w}_2 indicates respectively the first and second component of the
 550 vector \mathbf{w} and ∇^\perp stands for the normal gradient operator. Applying the scaling
 551 (12) to the two expressions above and introducing the dimensionless dispersion
 552 parameter $\mu = \frac{D_0}{L_0}$, we can state that $\mathbb{T}(\mathbf{w}) = \mu^2 \mathbb{T}'(\mathbf{w})$ and $\mathbb{Q}(\mathbf{w}) = \frac{\mu^2}{L_0} \mathbb{Q}'(\mathbf{w})$.
 553 Equation (5c), written in terms of dimensionless variables, then becomes (still
 554 primes are dropped for clarity):

$$(\mathbb{I} + \mu^2 \mathbb{T}) \boldsymbol{\psi} = \mu^2 \mathbb{T} \left(\frac{1}{K\mathcal{L}} \delta_0^2 \nabla \zeta - K \frac{\epsilon_0 \phi_0}{\delta_0} \frac{\mathbf{u}|\mathbf{u}|}{D} \right) - \mu^2 \mathbb{Q} \left(\frac{K}{\mathcal{L}} \epsilon_0 \mathbf{u} \right). \quad (15)$$

555 Equation (15) can be rearranged as follows:

$$\boldsymbol{\psi} = \mu^2 (\mathbb{I} + \mu^2 \mathbb{T})^{-1} \left[\mathbb{T} \left(\frac{1}{K\mathcal{L}} \delta_0^2 \nabla \zeta - K \frac{\epsilon_0 \phi_0}{\delta_0} \frac{\mathbf{u}|\mathbf{u}|}{D} \right) - \mathbb{Q} \left(\frac{K}{\mathcal{L}} \epsilon_0 \mathbf{u} \right) \right], \quad (16)$$

556 showing that $\boldsymbol{\psi} = \mu^2 \boldsymbol{\Psi}$.

557 The final form of scaled SGN system will thus read:

$$\frac{\partial \zeta}{\partial t} + \frac{K}{\mathcal{L}} (\epsilon_0 \mathbf{u} \nabla \zeta + D \nabla \cdot \mathbf{u}) = 0, \quad (17a)$$

$$\frac{\partial \mathbf{u}}{\partial t} + \frac{K}{\mathcal{L}} \epsilon_0 (\mathbf{u} \cdot \nabla) \mathbf{u} + \frac{1}{K\mathcal{L}} \delta_0^2 \nabla \zeta + K \frac{\epsilon_0 \phi_0}{\delta_0} \frac{\mathbf{u}|\mathbf{u}|}{D} = \mu^2 \boldsymbol{\Psi}, \quad (17b)$$

$$\boldsymbol{\Psi} = (\mathbb{I} + \mu^2 \mathbb{T})^{-1} \left[\mathbb{T} \left(\frac{1}{K\mathcal{L}} \delta_0^2 \nabla \zeta - K \frac{\epsilon_0 \phi_0}{\delta_0} \frac{\mathbf{u}|\mathbf{u}|}{D} \right) - \mathbb{Q} \left(\frac{K}{\mathcal{L}} \epsilon_0 \mathbf{u} \right) \right]. \quad (17c)$$

558 Appendix B: Landward boundary conditions

559 Imposing correctly the landward boundary condition (b.c.) is not a trivial
 560 operation. Up to the authors knowledge, there is not an efficient and systematic
 561 method to impose an outflow conditions in the presence of friction and conver-
 562 gence. In this appendix a sensitivity analysis has been performed in order to
 563 quantify the influence of the inexact b.c. that has been implemented for this

564 study (*cf.* section 3.3). Two tests have been conducted: one for a low and
 565 the other for a high value of the nonlinear parameter ϵ_0 , respectively $\epsilon_0 = 0.1$
 566 and $\epsilon_0 = 0.7$. We compare two solutions: one computed by setting the outflow
 567 b.c. at the location $x = 5L_b$, the other, considered as a reference, derived by
 568 imposing a wall b.c. at the further distance $x = 8L_b$, where the tidal wave is as-
 569 sumed to be completely dissipated. Figure 14 shows the time evolution profiles
 570 of the non-dimensional free surface and velocity at different positions along the
 571 channel. In order to measure the deviation from the reference solution we use
 572 the L_2 -norm $\frac{\|\zeta - \zeta_{ref}\|_{L_2}}{\|\zeta_{ref}\|_{L_2}}$. At the station $x = 3L_b$, the percentage values of the
 573 deviation are 3.3% for ζ and 3.98% for u in the case with $\epsilon_0 = 0.1$, while being
 574 respectively 5.27% and 7.67% in the case with $\epsilon_0 = 0.7$.

575 Toffolon [21] revealed the difficulties of imposing such conditions. He con-
 576 sidered two limit cases: the reflecting barrier and the transparent condition.
 577 On the former, a wall boundary condition was imposed at the end of the chan-
 578 nel, which determined a complete reflection of the wave. The latter condition,
 579 instead, referred to a situation where the tidal wave exited from the compu-
 580 tational domain without being deformed or reflected (transparent b.c.). This
 581 condition was implemented by replacing, on the last cells of the domain, mass
 582 and momentum conservation laws with a scalar advection equation for each con-
 583 servative variable, characterized by an advection speed equal to the outgoing
 584 eigenvalue. Even though, the need of considering a longer estuary in order to
 585 vanish the influence of the boundary on the solution, remained.

586 Figure 15 shows the comparison with the solution performed by implementing
 587 the transparent boundary condition used in [21]. The percentage deviations
 588 from the reference are of the same order of magnitude as those recovered us-
 589 ing our approach and, most importantly, the two approaches provide identical
 590 topologies for both the water depth and the velocity. The results of our study
 591 are thus independent from the choice of the method used.

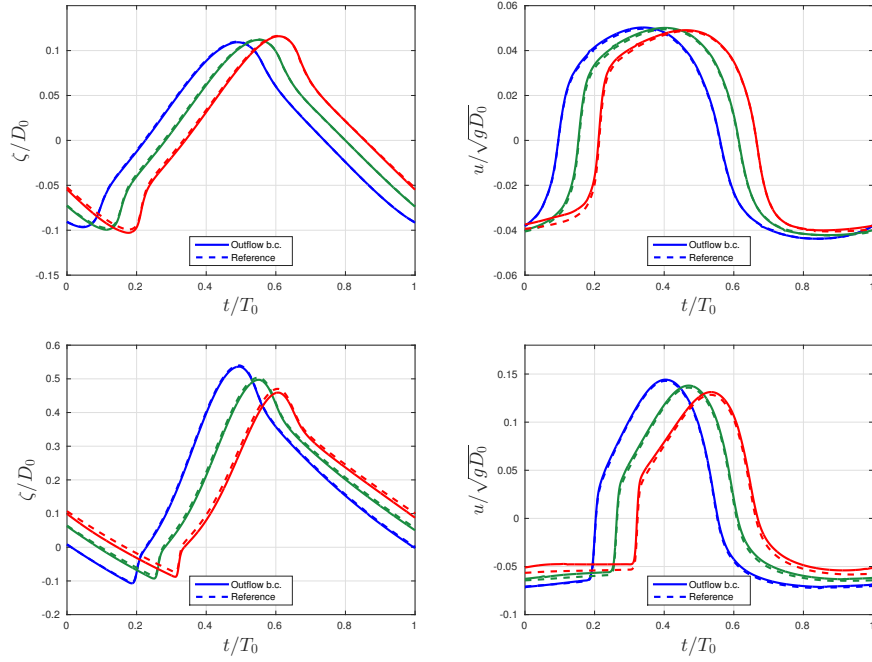


Figure 14: Time evolution profiles of the non-dimensional free surface (left) and velocity (right) measured at $x = 2L_b$ (—), $x = 2.5L_b$ (—) and $x = 3L_b$ (—) for the two test cases performed with $\epsilon_0 = 0.1$ (top) and $\epsilon_0 = 0.7$ (bottom). In the two computations ϕ_0 has been set constant and equals to $\phi_0 = 35$. Continuous lines represent the results obtained by using absorbing landward b.c. by means of the homogeneous NSW invariants at $x = 5L_b$; while dashed lines were obtained by imposing wall b.c. at $x = 8L_b$.

592 Acknowledgments

593 Experiments presented in this paper were carried out using the PlaFRIM
 594 experimental platform, developed under the INRIA PlaFRIM development ac-
 595 tion with support from LABRI and IMB and other entities: Conseil Régional
 596 d'Aquitaine, FeDER, Université de Bordeaux and CNRS. This work was par-
 597 tially funded by the TANDEM contract, reference ANR-11-RSNR-0023-01 of
 598 the French *Programme Investissements d'Avenir*.

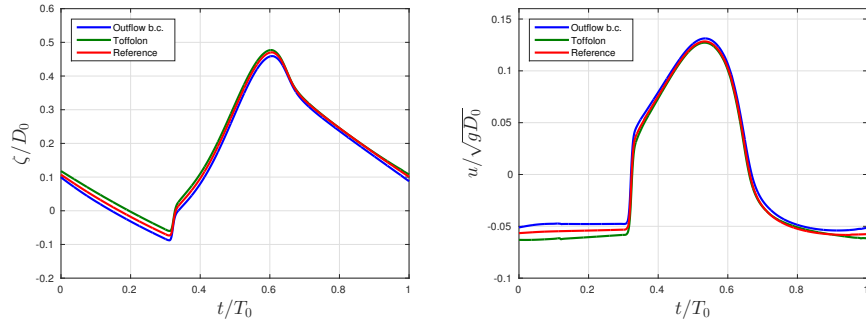


Figure 15: Time evolution profiles of the non-dimensional free surface (left) and velocity (right) measured at $x = 3L_b$, obtained by setting the absorbing homogeneous b.c. (—) and the transparent b.c. of [21] (—). The red curve (—) represents the reference solution computed by imposing wall b.c. on a longer domain of $L = 8L_b$ ($\epsilon_0 = 0.7$ and $\phi_0 = 35$).

599 References

- 600 [1] S. Lanzoni, G. Seminara, On tide propagation in convergent estuaries, *J.*
601 *Geophys. Res.* 103 (1998) 30793–30812.
- 602 [2] M. Toffolon, G. Vignoli, M. Tubino, Relevant parameters and finite am-
603 plitude effects in estuarine hydrodynamics, *J. Geophys. Res.* 111 (2006)
604 1–17.
- 605 [3] P. Bonneton, N. Bonneton, J. P. Parisot, B. Castelle, Tidal bore dy-
606 namics in funnel-shaped estuaries, *J. Geophys. Res.* 120 (2015) DOI:
607 10.1002/2014JC010267.
- 608 [4] A. Munchow, R. W. Garvin, Nonlinear barotropic tides and bores in estu-
609 aries, *Tellus* 43 (1991) 246–256.
- 610 [5] H. Cai, H. H. G. Savenije, M. Toffolon, Linking the river to the estuary:
611 influence of river discharge on tidal damping, *Hydrol. Earth Syst. Sci.* 18
612 (2014) 287–304.
- 613 [6] H. H. G. Savenije, *Salinity and tides in alluvial estuaries*, 2nd Edition, 2012.

- 614 [7] D. H. Peregrine, Calculations of the development of an undular bore,
615 J.Fluid Mech. 25 (1966) 321–330.
- 616 [8] P. A. Madsen, H. J. Simonsen, C. H. Pan, Numerical simulation of tidal
617 bores and hydraulic jumps, Coast. Eng. 52 (2005) 409–433.
- 618 [9] C. H. Pan, H. Lu, 2d numerical simulation of tidal bore on Qiantang river
619 using KFVS scheme, Vol. 32, 2010.
- 620 [10] A. E. Green, P. M. Naghdi, A derivation of equations for wave propagation
621 in water of variable depth, J.Fluid Mech. 78 (1976) 237–246.
- 622 [11] M. Tissier, P. Bonneton, F. Marche, F. Chazel, D. Lannes, Nearshore dy-
623 namics of tsunami-like undular bores using a fully nonlinear Boussinesq
624 model, J. Coast. Res. 64 (2011) 603–607.
- 625 [12] G. A. El, R. H. Grimshaw, N. F. Smyth, Unsteady undular bores in fully
626 nonlinear shallow water theory, Phys. Fluids 18(2).
- 627 [13] P. Bonneton, A. G. Filippini, L. Arpaia, N. Bonneton, M. Ricchiuto, Con-
628 ditions for tidal bore formation in convergent alluvial estuaries, Estuarine,
629 Coastal and Shelf Science, doi:10.1016/j.ecss.2016.01.019.
- 630 [14] G. Davies, C. D. Woodroffe, Tidal estuary width convergence: Theory
631 and form in North Australian estuaries, Earth Surf. Process. Landforms 35
632 (2010) 737749.doi: 10.1002/esp.1864.
- 633 [15] C. T. Friedrichs, D. G. Aubrey, Tidal propagation in strongly
634 convergent channels, J. Geophys. Res. 99(C2) (1994) 33213336.doi:
635 10.1029/93JC03219.
- 636 [16] A. C. Horrevoets, H. H. G. Savenije, J. N. Schuurman, S. Graas, The
637 influence of river discharge on tidal damping in alluvial estuaries, J. Hydrol.
638 294 (2004) 213–228.
- 639 [17] H. H. G. Savenije, M. Toffolon, J. Haas, M. Veling, Analytical description
640 of tidal dynamics in convergent estuaries, J. Geophys. Res. 113 (2008) 1–18.

- 641 [18] P. Winckler, P. L. Liu, Long waves in a straight channel with non-uniform
642 cross-section, *J.Fluid Mech.* 770 (2015) 156–188.
- 643 [19] P. Bonneton, F. Chazel, D. Lannes, F. Marche, M. Tissier, A splitting
644 approach for the fully nonlinear and weakly dispersive Green-Naghdi model,
645 *J.Comp.Phys.* 230(4) (2011) 1479–1498.
- 646 [20] A. G. Filippini, M. Kazolea, M. Ricchiuto, A flexible genuinely non-
647 linear approach for nonlinear wave propagation, breaking and run-up,
648 *J.Comp.Phys.* 310 (2016) 381417.
- 649 [21] M. Toffolon, Hydrodynamics and morphodynamics of tidal channels, Ph.D.
650 thesis, Università degli studi di Trento (2002).
- 651 [22] J. T. Kirby, G. Wei, Q. Chen, FUNWAVE 1.0, Fully Nonlinear Boussinesq
652 Wave Model Documentation and User’s Manual, Tech. Rep. CACR-98-06,
653 University of Delaware (September 1998).
- 654 [23] G. Wei, J. T. Kirby, A. Sinha, Generation of waves in Boussinesq models
655 using a source function method, *Coast.Eng.* 36 (1999) 271–299.
- 656 [24] M. A. Walkley, A numerical method for extended Boussinesq shallow-water
657 wave equations, Ph.D. thesis, University of Leeds (1999).
- 658 [25] Y. Zhang, A. B. Kennedy, N. Panda, C. Dawson, J. J. Westerink,
659 Generating-absorbing sponge layers for phase-resolving wave models,
660 *Coast.Eng.* 84 (2014) 1–9.
- 661 [26] R. Cienfuegos, E. Barthelémy, P. Bonneton, A fourth-order com-
662 pact finite volume scheme for fully nonlinear and weakly dispersive
663 Boussinesq-type equations. part II: Boundary conditions and validation,
664 *Int.J.Numer.Meth.Fluids* 53 (2007) 1423–1455.
- 665 [27] E. Wolanski, D. Williams, E. Hanert, The sediment trapping efficiency of
666 the macro-tidal Daly Estuary, tropical Australia, *Estuarine, Coastal and*
667 *Shelf Science* 69(1) (2006) 291–298.

- 668 [28] J. C. Winterwerp, Z. B. Wang, A. van Braeckel, G. van Holland, F. Kesters,
669 Man-induced regime shifts in small estuaries II: a comparison of rivers,
670 *Ocean Dynamics* 63(11-12) (2013) 1293–1306.
- 671 [29] H. H. G. Savenije, E. J. M. Veling, Relation between tidal damp-
672 ing and wave celerity in estuaries, *J. Geophys. Res.* 101 (2005)
673 doi:10.1029/2004JC002278.
- 674 [30] H. H. G. Savenije, A simple analytical expression to describe tidal damping
675 or amplification, *J. Hydrol.* 243 (2001) 205–215.
- 676 [31] G. Vignoli, M. Toffolon, M. Tubino, Non-linear frictional residual effects
677 on tide propagation, *Proceedings of XXX IAHR Congress* (2003) 291–298.
- 678 [32] H. Chanson, *Tidal Bores, Aegir, Aegir, Eagre, Mascaret, Pororoca: Theory*
679 *and Observations*, World Scientific, Singapore, 2012.